Research Square

Preprints are preliminary reports that have not undergone peer review.
They should not be considered conclusive, used to inform clinical practice,
or referenced by the media as validated information.

Optimization of the Seebeck coefficient and electrical conductivity in Sb_2Se_3/rGO nanocomposites by controlling the rGO contents

Muhammad Arif
Government College University Faisalabad
Sofia Akbar Tahir
Government College University Faisalabad
Khalid Mahmood
khalid_mahmood856@yahoo.com
Government College University Faisalabad

Research Article

Keywords: Sb2Se3/rGO composite, rGO contents, XRD, power factor

Posted Date: November 3rd, 2026

DOI: https://doi.org/10.21203/rs.3.rs-11401026/v1

License: This work is licensed under a Creative Commons Attribution 4.0 International License.
Read Full License

Additional Declarations: No competing interests reported.

Abstract

This manuscript reported a high power factor in Sb_2Se_3/rGO nanocomposites by optimizing the Seebeck coefficient and electrical conductivity. Pristine rGO and Sb_2Se_3 nanoparticles were synthesized by hydrothermal technique and subsequently composite was prepared by solid state reaction method using different contents (weight) of rGO ranging from10-40%. XRD data confirmed the graphitic carbon and orthorhombic structures of as grown rGO and Sb_2Se_3 nanoparticles respectively. The Sb_2Se_3/rGO nanocomposites sustained the orthorhombic structure but it found to be degraded with increasing the concentration of rGO. This degradation was further verified by performing the Raman and UV-Vis spectroscopic measurements. Seebeck data suggested that even the highest electrical conductivity of 35 S/cm for rGO and the highest value of Seebeck coefficient of 998 μV/K for Sb_2Se_3 nanoparticles resulted very poor power factors for both rGO and Sb_2Se_3 nanoparticles (0.6 and 0.8 μW/m.K^2 respectively). To optimize the electrical conductivity and the Seebeck coefficient, the concentration of rGO in Sb_2Se_3/rGO composite was varied and it was found that 10% rGO is suitable to achieve highest power factor of 2.4 μW/m.K^2. This reported power factor is supposed to be the highest value for Sb_2Se_3/rGO composite having 10% rGO reported in the literature according to the best of our knowledge.

1. Introduction

Global energy needs continue to grow each year, with total consumption estimate to approach nearly 5900 TWh by 2050. This rapid increase has intensified the need to explore and develop alternative energy sources that can reduce environmental impact and lower carbon emissions [1]. Thermoelectricity is supposed to be good alternative because it enable direct conversion of thermal energy into electrical energy through the Seebeck effect using thermoelectric materials [2–6]. The efficiency of any thermoelectric material can be judged by power factor along with figure of merit. The temperature-dependent power factor (PF) quantifies the electrical performance of a thermoelectric material as a function of temperature and is defined as $PF=S^2T/\rho$, Where S denotes the Seebeck coefficient, T represents the absolute temperature and ρ is electrical resistivity [7–10]. Consequently, maximizing the power factor requires the high Seebeck coefficient in combination with low electrical resistivity. In practice, this optimization is challenging because enhancements in the Seebeck coefficient are often accompanied by an increase in resistivity. Therefore, the optimization of carrier concentration in any thermoelectric material has fundamental importance to achieve maximum power factor [11]. Current research in thermos-electrics aims to enhance the power factor (PF) of advanced bulk materials, particularly through nanostructuring strategies. In such systems, enhanced phonon scattering can improve the Seebeck coefficient (S) by selectively filtering charge carriers based on their energy by promoting preferential scattering at interfacial charged defects [12, 13]. Moreover, doping serves as a key strategy for band gap engineering, where the intrinsic electronic band structure plays a crucial role in determining the performance of materials for thermoelectric, photovoltaic, and photo-electrochemical applications [14]. In recent years, there has been growing interest in identifying efficient and economically viable materials for energy-related applications, driven by the increasing need for

sustainable and renewable energy technologies [15–18]. The search for new semiconductor materials has increasingly emphasized compounds that offer an optimal combination of performance, cost-effectiveness, and environmental compatibility. Antimony selenide (Sb_2Se_3) has emerged as a promising material owing to its advantageous electronic properties, widespread availability, and low toxicity, making it suitable for diverse applications such as photovoltaics, thermo-electrics, and photodetectors [19–21]. Furthermore, the thermal stability of this material is very good which is essential for high reliability of thermoelectric module [22–24]. Despite its promising optoelectronic characteristics, the thermal behavior of Sb_2Se_3 has received limited attention, highlighting a notable knowledge gap that must be addressed to enable its practical applications in thermoelectric devices [24].

In this work, we present the synthesis of Sb_2Se_3/rGO nanocomposites by varying rGO contents in the range of 10–40% for thermoelectric applications. A specific concentration (10%) of rGO in the Sb_2Se_3 was found to be optimal because it yield a highest power factor of 2.4 μW/m.K^2 when compared with the as grown rGO and Sb_2Se_3 nanoparticles separately. The established argument was further supported by some additional measurements such as XRD, Raman spectroscopy and UV-Vis spectroscopy.

2. Experimental detail

The starting materials used for this study are graphite powder, sulfuric acid, hydrochloric acid, hydrazine, potassium permanganate ($KMnO_4$), ethanol, di water, antimony powder and selenium powder. All the materials purchased from Sigma Aldrich with 99.999% purity. Three step procedure was adopted to synthesize the required samples. During first step, Graphene oxide (GO) was synthesized using the modified Hummers method as a precursor for the preparation of reduced graphene oxide. In this process, 2g of graphite powder and 2g of sodium nitrate were dissolved in 50mL of concentrated sulfuric acid. The mixture was stirred at 350rpm while maintaining the temperature between 0–6°C using an ice bath for 3hours. After this period, 6g of $KMnO_4$ was gradually added while keeping the temperature between 15–20°C. The reaction was allowed to proceed for 1 hour. Subsequently, the ice bath was removed, and the temperature was raised to 35°C until the mixture turned dark in color. At next step, 100mL of deionized water was added drop-wise while maintaining the temperature at 90–95°C. Then, 10mL of hydrogen peroxide was added into the mixture to complete the reaction. The resulting precipitate was washed several times with deionized water and ethanol to remove impurities. The washed product was dried in an oven at 90°C for 8hours. Finally, the dried material was grind to obtain pure graphene oxide. After the synthesis of graphene oxide, the obtained GO powder was used to prepare reduced graphene oxide (rGO). For this purpose, 2g of GO powder was dissolved in 20mL of hydrazine monohydrate and stirred at 600rpm for 30minutes at room temperature. The reaction mixture was then heated in a water bath at 95°C for 45minutes to help the reduction process. After completion of the reaction, the precipitate was filtered and washed several times with deionized water and ethanol to remove residual impurities. The product was dried in an oven at 90°C for 8hours. Finally, the dried material was grind to obtain pure reduced graphene oxide. The complete flow diagram of whole process can be shown in Fig. 1.

During 2nd and 3rd steps, Sb_2Se_3 nano-particles and Sb_2Se_3/rGO nanocomposites were prepared. Initially, Sb_2Se_3 was synthesized in a 2:3 weight ratio using the solid-state reaction method. Subsequently, Sb_2Se_3-based rGO nanocomposites were prepared with different weight percentages of rGO. For this purpose, separate samples containing 10%, 20%, 30%, & 40% rGO were prepared using the same solid-state method. For thermoelectric measurements, pellets of each sample with weight of 400mg were prepared by applying a pressure of 3000psi using a homemade hydraulic press system.

The crystalline structure of the synthesized Sb_2Se_3-based rGO nanocomposites were investigated by X-ray diffraction (XRD) using a Bruker D8 Advance diffractometer (Germany). Raman spectroscopy was performed using a confocal micro-Raman mapping system and band gap was measured the DU-8200 UV-Vis spectrometer. The thermoelectric response of the synthesized samples was evaluated using a home-developed Seebeck measurement system. The Seebeck coefficient was determined by establishing a temperature gradient across the sample and measuring the resulting thermoelectric voltage.

3. Results and Discussions

Figure 2 demonstrated the X-ray diffraction (XRD) patterns of as grown rGO, Sb_2Se_3, and Sb_2Se_3/rGO nanocomposites having different rGO contents. The pristine rGO sample exhibits a broad diffraction peak at approximately $2\theta = 26°$, which can be assigned to the (002) reflection of graphitic carbon [25, 26]. The broad rGO XRD peak confirmed the disordered graphitic stacking which might be due the oxygen vacancies created during the growth process. Furthermore, the as grown Sb_2Se_3 sample exhibits distinct crystalline reflections at 28.7°, 29.8°, 40.0°, 42.0°, 45.3°, and 51.7° which are indexed to the corresponding crystallographic planes of orthorhombic Sb_2Se_3 as reported in the literature [26–28]. Upon incorporation of rGO, the characteristic XRD peaks of Sb_2Se_3 were also found in all composite samples, indicating that the crystalline framework of Sb_2Se_3 is preserved during composite formation, but the intensity of all XRD peaks was found to be decrease with increasing the rGO contents [29]. The relative low peak intensity suggested the degradation of crystal quality with increasing the rGO concentration in the composite. The degradation in the crystal quality with rGO content can be associated with the interaction between Sb_2Se_3 nanoparticles and the rGO sheets which can induce aggregation and local structural disorder. The poor crystal quality was further verified by observing the shift in main XRD peak towards higher 2theta with increasing rGO contents. According to Bragg's law, this shift can be associated with local structural distortion or interfacial stress generated through the intimate interaction between Sb_2Se_3 crystallites and rGO sheets. In conclusion, the XRD results confirm the coexistence of crystalline Sb_2Se_3 and the graphitic rGO phase without any apparent formation of additional crystalline impurity phases [26]. This interpretation agrees with previous reports showing intimate integration of nanosized Sb_2Se_3 with rGO resulted in the agglomeration and degradation in crystal quality [30].

The Raman spectra shown in Fig. 3 further supported the structural features identified by XRD for the Sb_2Se_3/rGO nanocomposites. A characteristic Raman mode observed at approximately 450cm^{-1} which is attributed to a vibrational mode of crystalline Sb_2Se_3, in agreement with previously reported Raman spectra of Sb_2Se_3 nanostructures [31]. With increasing rGO content, two more prominent bands emerged in the carbon-related region at approximately 1343 and 1600cm^{-1} which are assigned to the D and G bands of rGO, respectively [32]. It is well established fact the D band originates from defect-activated vibrations associated with structural disorder, whereas the G band corresponds to the in-plane vibrational mode of sp^2-hybridized of carbon atoms [33, 34]. The increasing strength of these bands with increasing contents of rGO may provides direct evidence for the incorporation of the carbonaceous phase into the Sb_2Se_3 matrix. This observation is consistent with the XRD results, where the broad carbon-related feature near 25.7° is accompanied by the characteristic diffraction reflections of orthorhombic Sb_2Se_3. The Raman and XRD results therefore provide complementary evidence that the rGO sheets are intimately integrated with Sb_2Se_3, where the carbon framework can restrict Sb_2Se_3 crystallite growth and generate a structurally heterogeneous interface. Similar Sb_2Se_3/rGO systems have demonstrated the coexistence of orthorhombic Sb_2Se_3 with characteristic D and G bands of rGO, supporting this interpretation [35].

The variation of band gap with respect to the rGO contents in Sb_2Se_3/rGO nanocomposites is shown in Fig. 4. As grown rGO and Sb_2Se_3 have band gaps of 1.75 and 2.12 eV respectively which were calculated using the UV-Vis data. The 2.01eV transition observed for Sb_2Se_3 is consistent with the higher-energy optical transition reported near 2.0eV, rather than its fundamental indirect band gap (~ 1.1-1.3eV) [36–38]. But the band gap starts decreasing when the rGO contents increases in the host matrix with values 2.08, 2.06, 2.02, and 2.01eV with 10, 20, 30, and 40% rGO concentration, respectively. The observed reduction in the band gap values with rGO concentration is related with defects and disorder caused by the rGO in Sb_2Se_3 host crystal which resulted in the small decrease of band gap.

The Seebeck coefficient of pristine rGO, Sb_2Se_3, and the Sb_2Se_3/rGO nanocomposites having different concentrations of rGO in the range of 10–40% is shown in the Fig. 5. Pristine Sb_2Se_3 exhibited the highest Seebeck coefficient of 998μV/K, which can be associated with its highly resistive semiconducting character and relatively low carrier concentration. Such high Seebeck values are consistent with previous experimental reports on Sb_2Se_3 nanostructures, where positive Seebeck coefficients of several hundred μV/K have been reported [39]. But the incorporation of rGO resulted in the sharp reduction of Seebeck coefficient to 449 μV/K at 10%, followed by a gradual increase to 30 μV/K at 40% rGO contents. This reduction can easily understand because the incorporation of rGO may enhance the carrier concentration in the host crystal of Sb_2Se_3 and due to the inverse dependence of carrier concentration and the Seebeck coefficient, this reduction is understandable. Furthermore, additional rGO contents introduce interfaces, crystallite refinement, and a defect-rich sp^2 carbon network, therefore these features facilitate carrier transport and consequently reduce the Seebeck coefficient [40–42].

The electrical conductivity data shown in Fig. 6 clearly exhibits an enhancement with increasing rGO content. It is also observed that Pristine Sb_2Se_3 possessed the lowest conductivity with a value of 0.5

S/cm whereas rGO hold the highest value of 35S/cm while the conductivity of the Sb_2Se_3/rGO composites increases progressively from 10 S/cm for 10%rGO to 30 S/cm for 40%rGO sample. This enhancement is attributed primarily to the gradual formation of interconnected rGO conductive pathways within the Sb_2Se_3 matrix, which facilitates carrier transport and reduces interparticle electrical resistance [43, 44]. The gradual increase in conductivity further demonstrated that rGO effectively improves the carrier concentration which is supposed to be the major contributor in the electrical conductivity. This argument is also supported by the decreasing trend of the Seebeck coefficient at high rGO contents loading [45].

The calculated power factor, PF = $S^2\sigma$, provides a combined assessment of the Seebeck coefficient and electrical conductivity [46]. Due to dependence of power factor on electrical conductivity and the Seebeck coefficient, the optimized values of these both parameters is very important to get the highest thermo-power. The pristine Sb_2Se_3 and rGO samples exhibit a low power factor of 0.6 and 0.9 μW/m.K^2 due to lowest Seebeck coefficient and electrical conductivity respectively (Fig. 7). But Sb_2Se_3/rGO composite having 10% rGO observed the highest value of 2.4 μW/m.K^2 due to moderate values of the Seebeck coefficient and electrical conductivity. This value is approximately 14 times higher than that of as grown rGO and Sb_2Se_3 samples. Therefore, the results demonstrate that excessive rGO contents can improves charge transport but does not necessarily enhance the overall thermoelectric power factor [46]. The optimum thermoelectric balance is obtained at 10%rGO, where conductive pathways and interfacial electronic effects provide a favorable combination of electrical conductivity and Seebeck coefficient.

4. Conclusion

In this paper, we have reported a high power factor of 2.4 μW/m.K^2 for Sb_2Se_3/rGO nano-composites having 10% concentration of rGO. The composite under investigation was prepared by solid state reaction method using hydrothermally synthesized rGO and Sb_2Se_3 nanoparticles. After structure and band gap analysis, Seebeck measurements were performed for all samples. The optimized values of the Seebeck coefficient and electrical conductivity for 10% rGO sample resulted in the high power factor which was not reported in the literature for this specific sample according to the best of our knowledge.

Declarations

Acknowledgments: N.A

Authors Contributions; Sofia Akbar Tahir and Khalid Mahmood has initiated the idea, Samples were prepared and characterize by Muhammad Arif

Funding; N.A

Conflict of Interest Statement; Authors have no conflict of interest

Data and code availability: No datasets were generated or analysed during the current study

Supplementary information: Not Applicable

Ethical Statement; Not Applicable

References

1. Daniel, J. E., Watkins, E., Jensen, M. S., Benton III, A., Rao, A., Bhattacharya, S., & Anderson, M. E. (2025). Impact of Cu-Site Dopants on Thermoelectric Power Factor for Famatinite (Cu3SbS4) Nanomaterials. *Electronic Materials*, *6*(3), 10.
2. Tritt, T. M. (2011). Thermoelectric phenomena, materials, and applications. *Annual review of materials research*, *41*(1), 433-448.
3. Shi, X., & Chen, L. (2016). Thermoelectric materials step up. *Nature materials*, *15*(7), 691-692.
4. Shi, X. L., Zou, J., & Chen, Z. G. (2020). Advanced thermoelectric design: from materials and structures to devices. *Chemical reviews*, *120*(15), 7399-7515.
5. Finn, P. A., Asker, C., Wan, K., Bilotti, E., Fenwick, O., & Nielsen, C. B. (2021). Thermoelectric materials: current status and future challenges. *Frontiers in electronic materials*, *1*, 677845.
6. Kumar, A., Bano, S., Govind, B., Bhardwaj, A., Bhatt, K., & Misra, D. K. (2021). A review on fundamentals, design and optimization to high ZT of thermoelectric materials for application to thermoelectric technology. *Journal of Electronic Materials*, *50*(11), 6037-6059.
7. Mamur, H., Dilmaç, Ö. F., Begum, J., & Bhuiyan, M. R. A. (2021). Thermoelectric generators act as renewable energy sources. *Cleaner Materials*, *2*, 100030.
8. Olabi, A. G., Al-Murisi, M., Maghrabie, H. M., Yousef, B. A., Sayed, E. T., Alami, A. H., & Abdelkareem, M. A. (2022). Potential applications of thermoelectric generators (TEGs) in various waste heat recovery systems. *International Journal of Thermofluids*, *16*, 100249.
9. Giri, K., Wang, Y. L., Chen, T. H., & Chen, C. H. (2022). Challenges and strategies to optimize the figure of merit: Keeping eyes on thermoelectric metamaterials. *Materials Science in Semiconductor Processing*, *150*, 106944.
10. Yan, Q., & Kanatzidis, M. G. (2022). High-performance thermoelectrics and challenges for practical devices. *Nature materials*, *21*(5), 503-513.
11. Shi, X., & Chen, L. (2016). Thermoelectric materials step up. *Nature materials*, *15*(7), 691-692.
12. Rowe, D. M., & Min, G. (1994, August). Multiple potential barriers as a possible mechanism to increase the Seebeck coefficient and electrical power factor. In *AIP Conference Proceedings* (Vol. 316, No. 1, pp. 339-342). American Institute of Physics.
13. Puneet, P., Podila, R., Karakaya, M., Zhu, S., He, J., Tritt, T. M., ... & Rao, A. M. (2013). Preferential scattering by interfacial charged defects for enhanced thermoelectric performance in few-layered n-type Bi2Te3. *Scientific reports*, *3*(1), 3212.

14. Dehkordi, A. M., Zebarjadi, M., He, J., & Tritt, T. M. (2015). Thermoelectric power factor: Enhancement mechanisms and strategies for higher performance thermoelectric materials. *Materials Science and Engineering: R: Reports*, *97*, 1-22.
15. Wang, Z., Bae, S., Baljozović, M., Adams, P., Yong, D., Service, E., ... & Tilley, S. D. (2024). One-step hydrothermal synthesis of Sn-doped Sb2Se3 for solar hydrogen production. *ACS catalysis*, *14*(13), 9877-9886.
16. Farhana, M. A., Manjceevan, A., & Bandara, J. (2023). Recent advances and new research trends in Sb2S3 thin film based solar cells. *Journal of Science: Advanced Materials and Devices*, *8*(1), 100533.
17. Carey, J. J., Allen, J. P., Scanlon, D. O., & Watson, G. W. (2014). The electronic structure of the antimony chalcogenide series: Prospects for optoelectronic applications. *Journal of Solid State Chemistry*, *213*, 116-125.
18. Surucu, G., Bal, E., Gencer, A., Parlak, M., & Surucu, O. (2024). Performance analysis of CuSbSe2 thin-film solar cells with Cd-free window layers. *Materials Letters*, *363*, 136296.
19. Bosio, A., Foti, G., Pasini, S., & Spoltore, D. (2023). A review on the fundamental properties of Sb2Se3-based thin film solar cells. *Energies*, *16*(19), 6862.
20. Terlemezoglu, M. (2024). Structural, morphological, and temperature-tuned bandgap properties of single-step thermally evaporated Sb2Se3 thin films. *Applied Physics A*, *130*(4), 251.
21. Chen, C., Li, W., Zhou, Y., Chen, C., Luo, M., Liu, X., ... & Tang, J. (2015). Optical properties of amorphous and polycrystalline Sb2Se3 thin films prepared by thermal evaporation. *Applied Physics Letters*, *107*(4).
22. Vidal-Fuentes, P., Guc, M., Becerril-Romero, I., Sylla, D., Alcobe, X., Sanchez, Y., ... & Izquierdo-Roca, V. (2021). Insights on the Thermal Stability of the Sb2Se3 Quasi-1D Photovoltaic Technology. *Solar RRL*, *5*(10), 2100517.
23. Niu, S., Milam-Guerrero, J., Zhou, Y., Ye, K., Zhao, B., Melot, B. C., & Ravichandran, J. (2018). Thermal stability study of transition metal perovskite sulfides. *Journal of Materials Research*, *33*(24), 4135-4143.
24. Altuntas, G., Isik, M., Surucu, G., Parlak, M., & Surucu, O. (2025). Exploring the Thermal Stability of Sb2Se3 for Potential Applications through Advanced Thermal Analysis Methods. *ACS omega*.
25. Alkhouzaam, A., Abdelrazeq, H., Khraisheh, M., AlMomani, F., Hameed, B. H., Hassan, M. K., ... & Selvaraj, R. (2022). Spectral and structural properties of high-quality reduced graphene oxide produced via a simple approach using tetraethylenepentamine. *Nanomaterials*, *12*(8), 1240.
26. Hu, L., Pan, J., Zhao, P., Shi, G., Wang, B., & Huang, F. (2022). A new method of synthesis of Sb2Se3/rGO as a high-rate and low-temperature anode for sodium–ion batteries. *Materials Advances*, *3*(8), 3554-3561.
27. https://www.scribd.com/document/897413313/Sb2Se3
28. Khandare, L. N., Gunjal, K., Bhosale, S. R., Bankar, P., & Chaure, N. B. (2025). High-performance supercapacitors based on Sb2Se3-rGO composite materials for advanced energy storage. *Journal of Alloys and Compounds*, *1021*, 179504.

29. Kusumandari, K., Karimah, L. S., Mufidah, R. I., Prasetya, N. P., Saraswati, T. E., Masruroh, M., ... & Isnaeni, I. (2025). Characteristic improvement of reduced graphene oxide from battery waste synthesized using modified Hummer's method. *Journal of Nanotechnology*, *2025*(1), 9919174.
30. Himabindu, B., Devi, N. L., & Kanth, B. R. (2021). Microstructural parameters from X-ray peak profile analysis by Williamson-Hall models; A review. *Materials Today: Proceedings*, *47*, 4891-4896.
31. Tian, Y., Sun, Z., Zhao, Y., Tan, T., Liu, H., & Chen, Z. (2018). One-Dimensional Sb2Se3 Nanorods Synthesized through a Simple Polyol Process for High-Performance Lithium-Ion Batteries. *Journal of Nanomaterials*, *2018*(1), 4273945.
32. Sadek, R., Sharawi, M. S., Dubois, C., Tantawy, H., & Chaouki, J. (2022). Superior quality chemically reduced graphene oxide for high performance EMI shielding materials. *RSC advances*, *12*(35), 22608-22622.
33. Zimniak, Z., Tylus, W., Borak, B., Pachnicz, M., Rutkowska-Gorczyca, M., Wróblewski, R., ... & Dusza, D. (2026). Three-dimensional bulk reduced graphene oxide coatings with strong metal adhesion via cold plasma and pulsed current. *Scientific Reports*, *16*(1), 6598.
34. Alves, T., Mota, W. S., Barros, C., Almeida, D., Komatsu, D., Zielinska, A., ... & Chaud, M. V. (2024). Review of scientific literature and standard guidelines for the characterization of graphene-based materials. *Journal of Materials Science*, *59*(32), 14948-14980.
35. Chong, S., Ma, M., Yuan, L., Qiao, S., Dong, S., Liu, H., & Dou, S. (2023). Hierarchical encapsulation and rich sp2 N assist Sb2Se3-based conversion-alloying anode for long-life sodium-and potassium-ion storage. *Energy & Environmental Materials*, *6*(6), e12458.
36. Jayswal, N. K., Rijal, S., Subedi, B., Subedi, I., Song, Z., Collins, R. W., ... & Podraza, N. J. (2021). Optical properties of thin film Sb2Se3 and identification of its electronic losses in photovoltaic devices. *Solar Energy*, *228*, 38-44.
37. Zhang, S., Wang, H., Kirchner, M. M., Liu, J., Luo, H., Ren, Y., ... & Lei, W. (2022). Ultrathin Sb2Se3 nanowires for polarimetric imaging photodetectors with a high signal/noise ratio. *Advanced Materials Interfaces*, *9*(17), 2200448.
38. Tene, T., Jiménez-Gaona, Y., Campoverde-Santos, D. K., Cevallos, Y., La Pietra, M., Vacacela Gomez, C., ... & Bellucci, S. (2023). Tunable optical and semiconducting properties of eco-friendly-prepared reduced graphene oxide. *Frontiers in Chemistry*, *11*, 1267199.
39. Ko, T. Y., Shellaiah, M., & Sun, K. W. (2016). Thermal and thermoelectric transport in highly resistive single Sb2Se3 nanowires and nanowire bundles. *Scientific reports*, *6*(1), 35086.
40. Yemata, T. A., Kyaw, A. K. K., Zheng, Y., Xu, J., Chin, W. S., Zhu, Q., & Hayashi, Y. (2025). Interface engineering in polymer thermoelectric composites: harnessing energy-filtering effects to overcome the Seebeck-conductivity trade-off. *Journal of Materials Chemistry A*, *13*(42), 35976-35998.
41. Aishwarya, K., Rajavardhini, R., Maruthasalamoorthy, S., Mani, J., Nirmala, R., Anbalagan, G., & Rangaswamy, N. (2024). NiMoO4/Reduced Graphene Oxide Nanocomposites for Thermoelectric Power Generation. *ACS Applied Nano Materials*, *7*(20), 23568-23579.

42. Katsantonis, S. N., & Tsamis, C. (2025). 3D-printed lattice structures for thermoelectric devices–a review. *Journal of Materials Chemistry A*, *13*(34), 27794-27806.
43. Monir, M. S. I., Rahman, A., Saha, P., Rahman, I., & Mahiuddin, M. (2026). Towards greener reduced graphene oxide: a critical review of environmentally driven reduction strategies. *RSC advances*, *16*(3), 2044-2061.
44. Rathi, V., Singh, K., Parmar, K. P. S., Brajpuriya, R. K., & Kumar, A. (2024). Improved thermoelectric performance of PEDOT: PSS/Bi2Te3/reduced graphene oxide ternary composite films for energy harvesting applications. *RSC advances*, *14*(47), 34883-34892.
45. Xue, X., Li, S., & Zhu, M. (2025). Recent progress in graphene-based materials for thermoelectric applications. *RSC advances*, *15*(33), 26919-26942.
46. Yuan, X., Zhao, Y., Ni, J., & Dai, Z. (2026). Progress in materials with high thermoelectric properties: A review. *Progress in Natural Science: Materials International*.

Figures

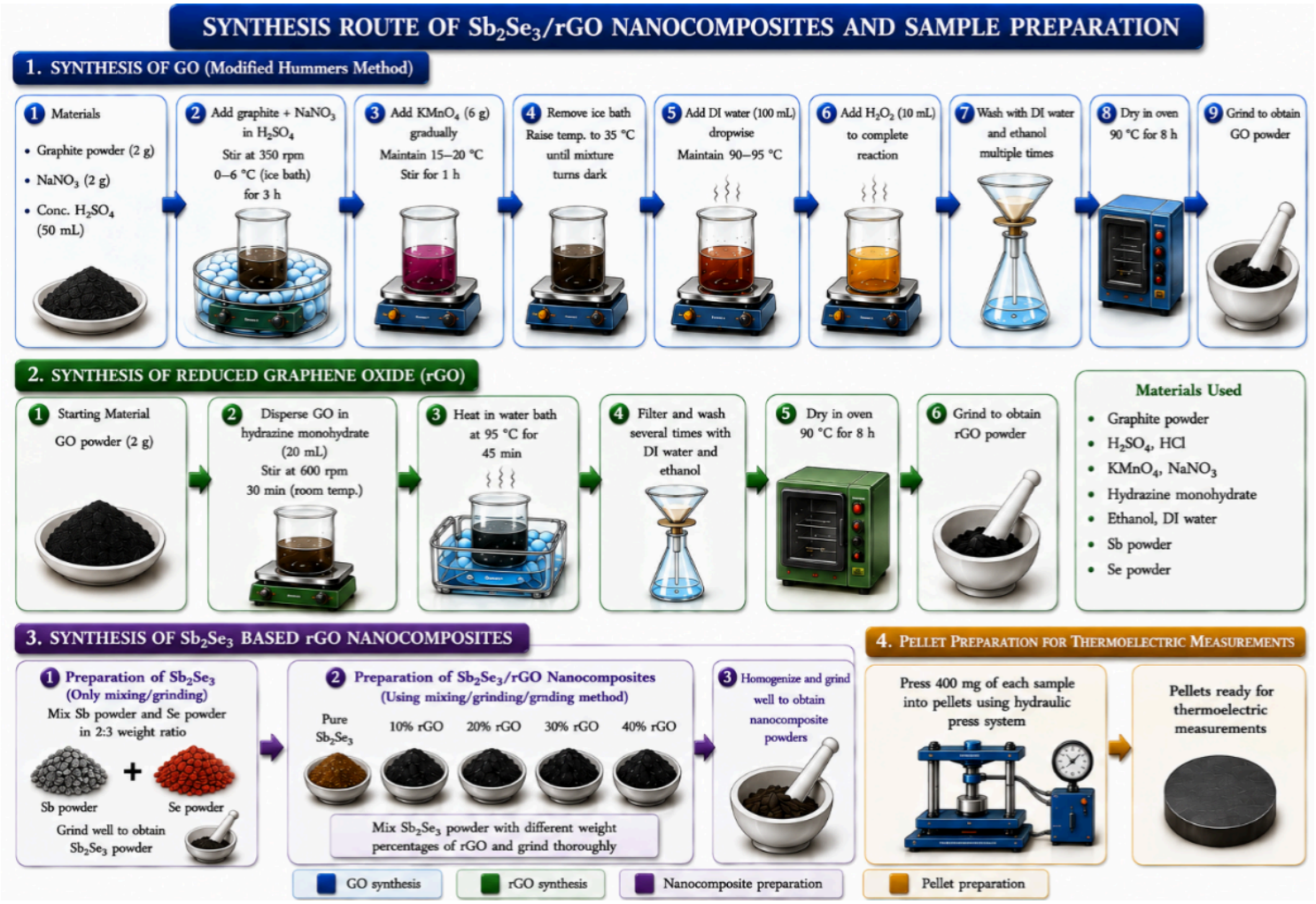


Figure 1

Flow chart of the synthesis process of rGO, Sb_2Se_3 and rGO/Sb_2S_3 nanocomposites

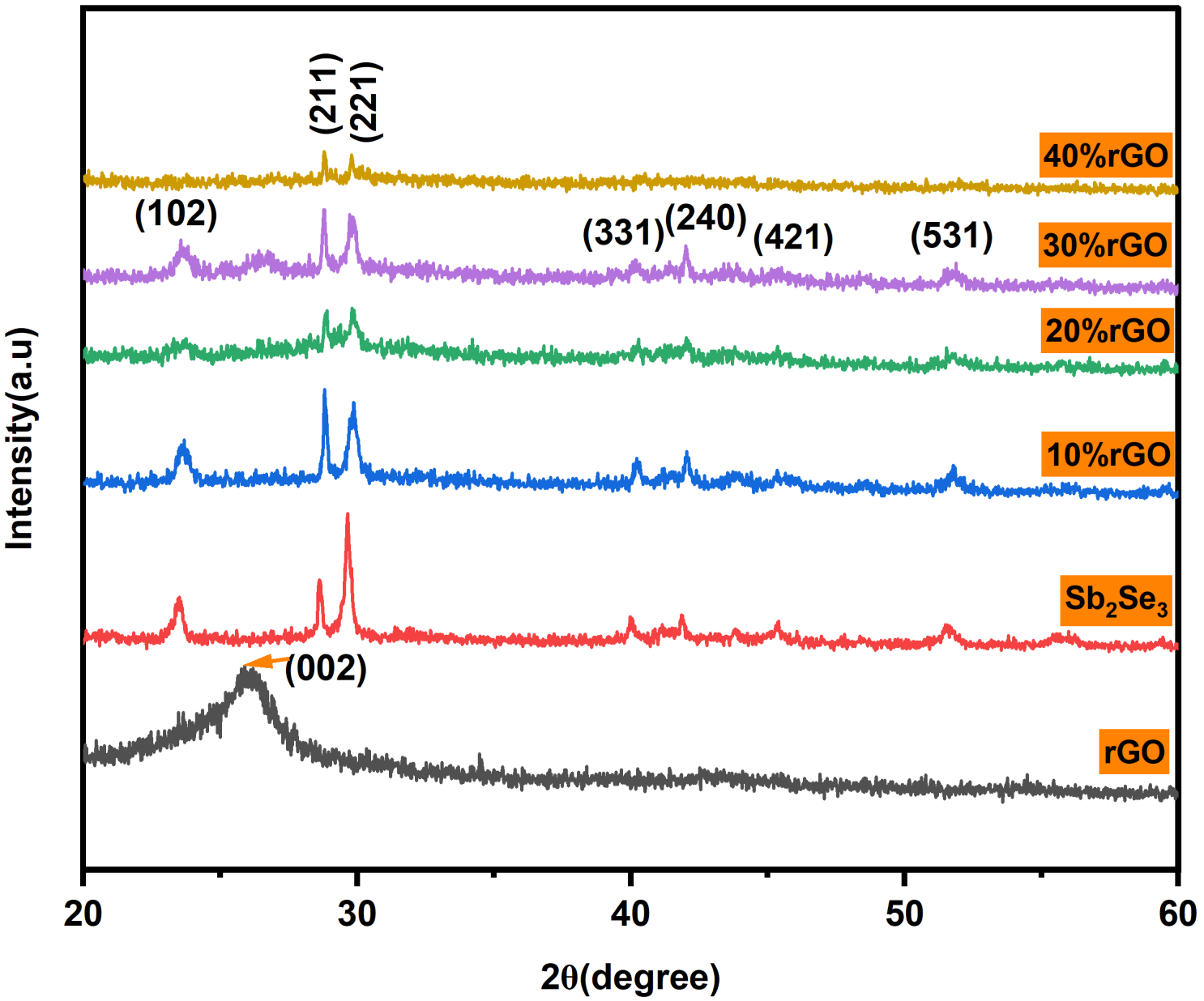


Figure 2

XRD patterns of rGO, Sb_2S_3, and their Composites

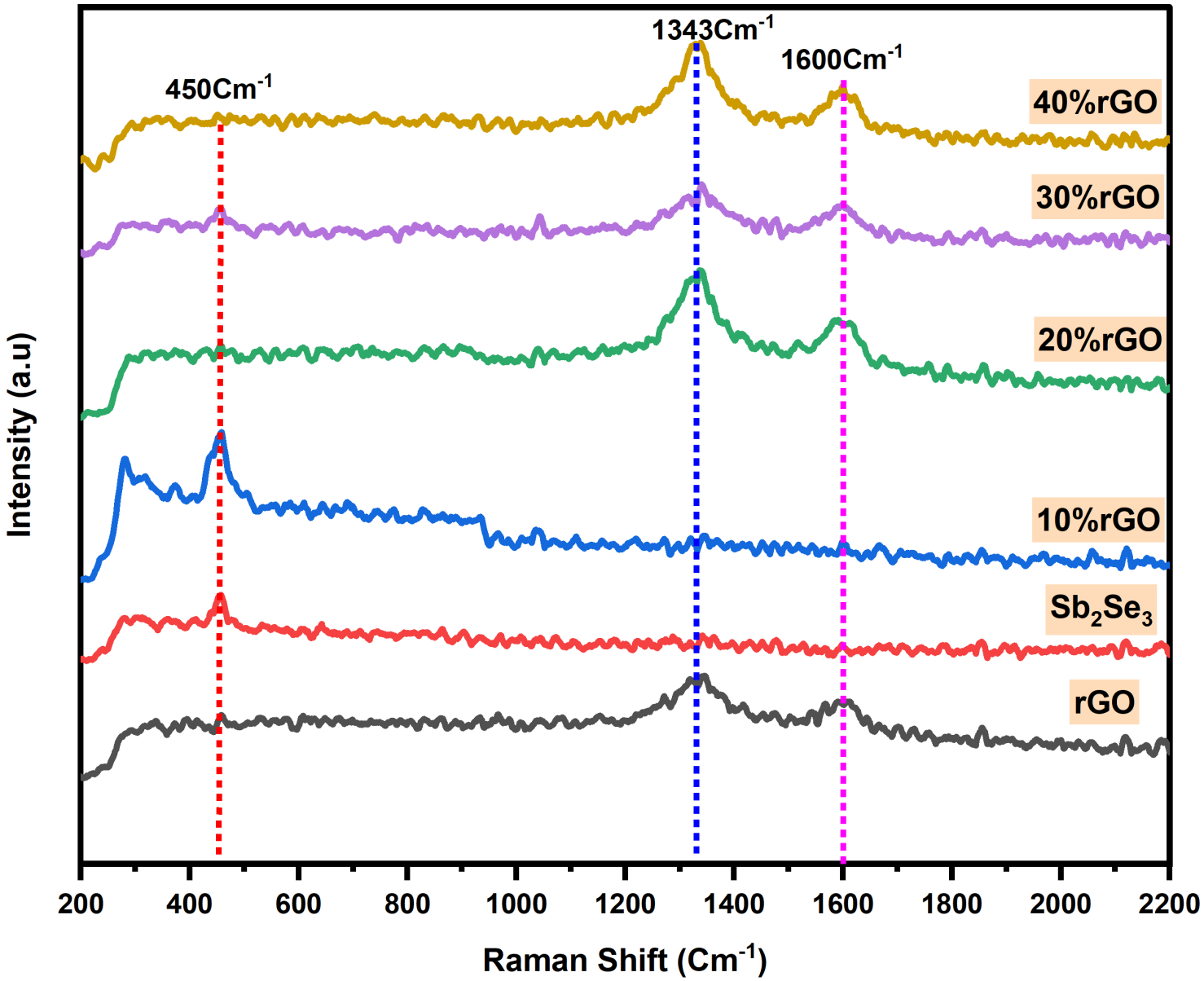


Figure 3

Raman spectra of as grown rGO, Sb_2S_3, and $Sb_2Se_{3/}$rGO composites having different concentration of rGO ranging from 10-40%

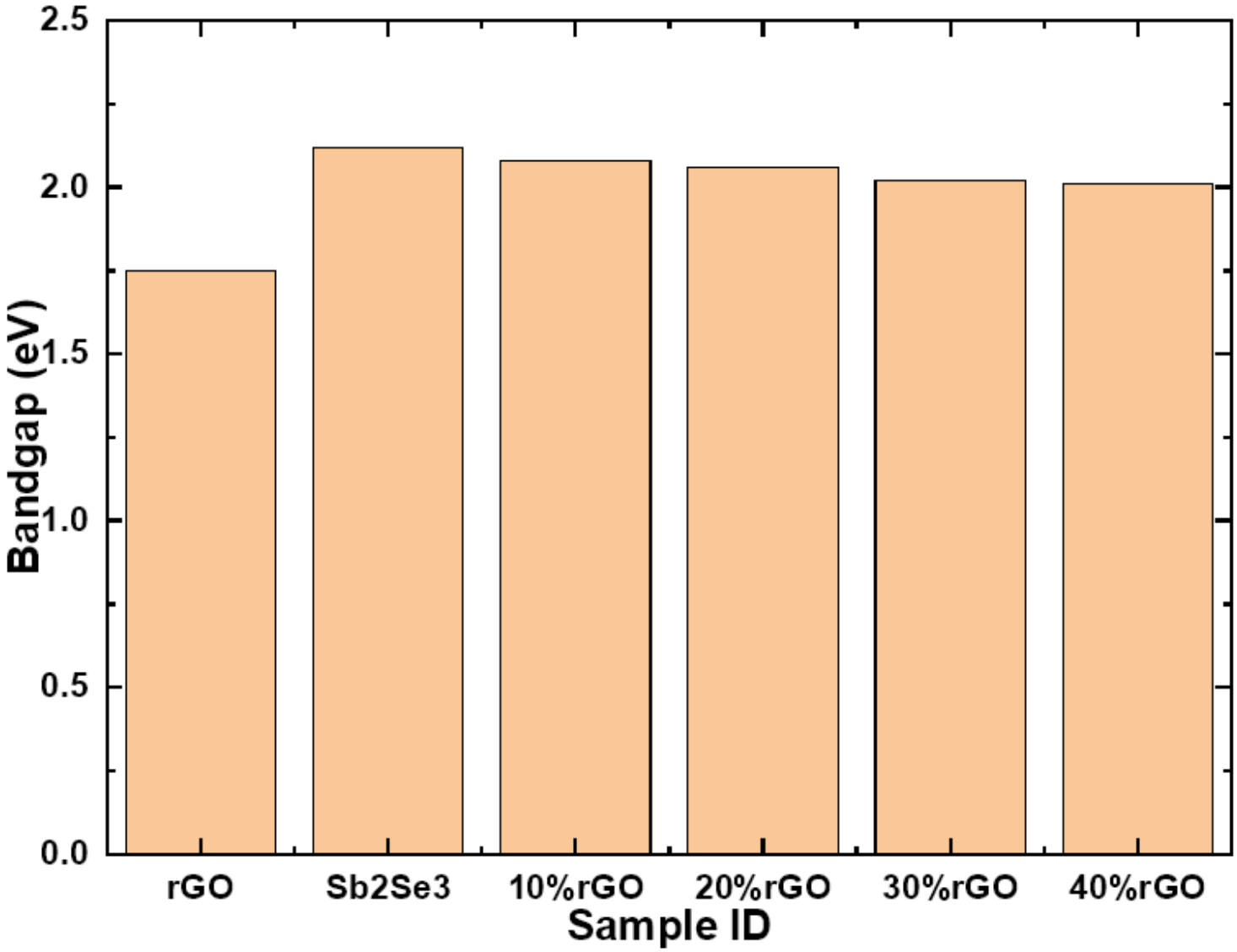


Figure 4

Band gap (eV) graph of rGO, Sb_2S_3, and their Composites having different concentrations of rGO atoms

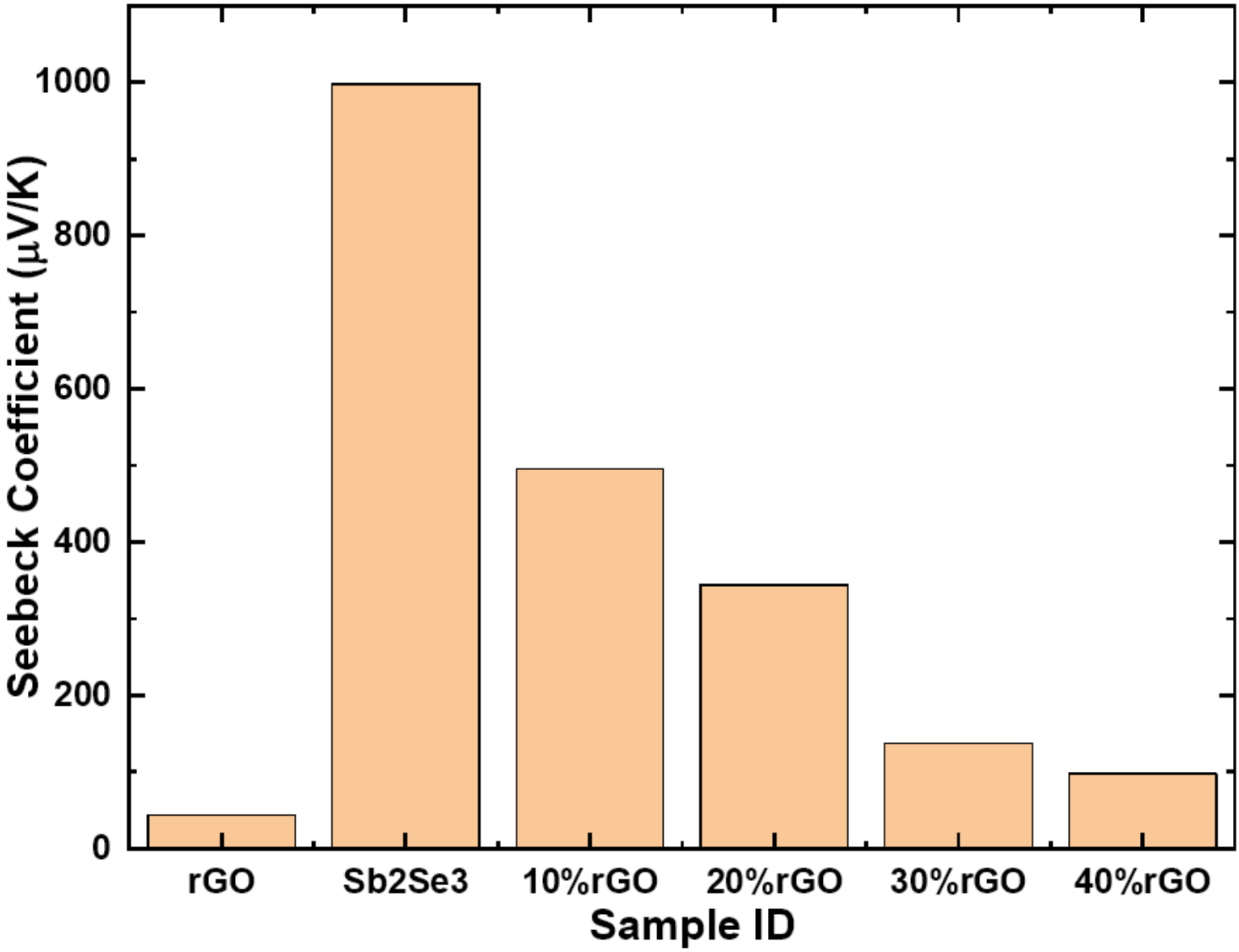


Figure 5

demonstrated the Seebeck coefficient of as grown rGO, Sb_2S_3 and effect of rGO concentration on the Seebeck coefficient of Sb_2Se_3/rGO nanocomposites

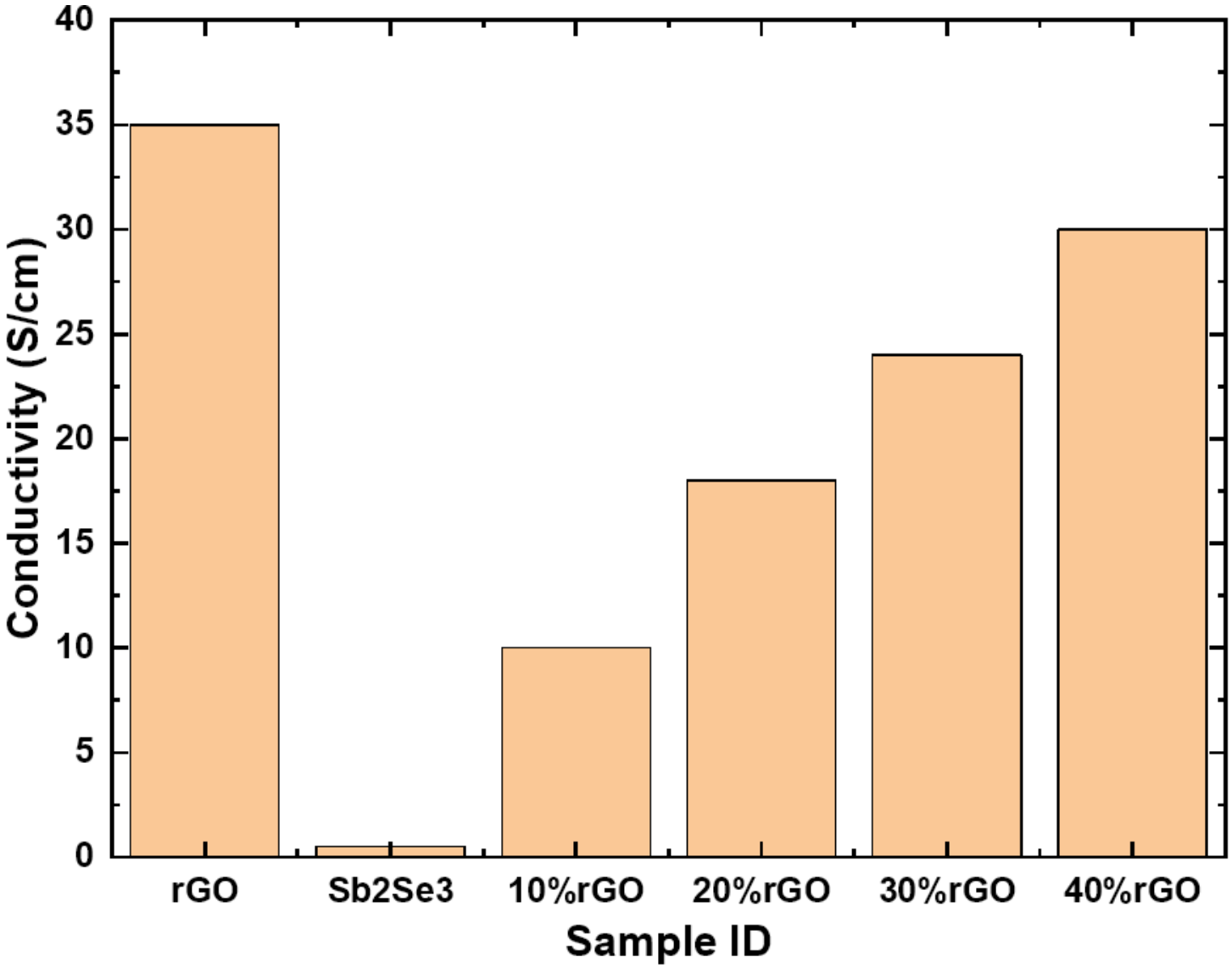


Figure 6

represents the electrical Conductivity data of rGO, Sb_2S_3 and its variation with rGO contents in Sb_2Se_3/rGO composites.

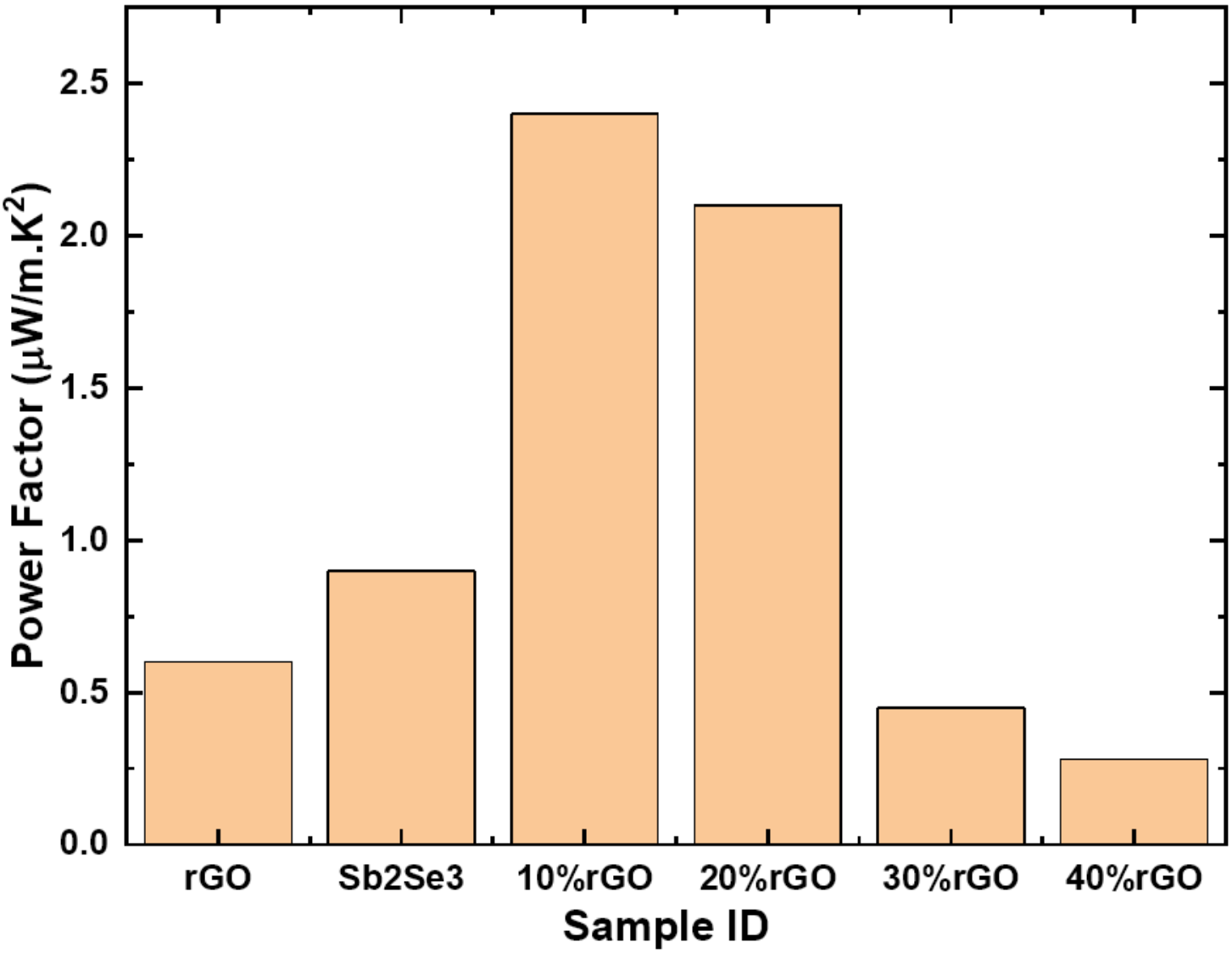


Figure 7

Power Factor graph of pure rGO, Sb_2S_3, and Sb_2Se_3 Composites having rGO contents in the range of 10-40% with a step of 10%